Tensile Behaviors of Double Network Hydrogels with Varied First Network Topological and Chemical Structures

Feixue Lu[1], Tasuku Nakajima[2,3], Yong Zheng[2], Hailong Fan[2], Jian Ping Gong[2,3]**

[1]*Graduate School of Life Science, Hokkaido University, Sapporo 001-0021, Japan.*

[2]*Institute for Chemical Reaction Design and Discovery (WPI-ICReDD), Hokkaido University, Sapporo 001-0021, Japan.*

[3]*Faculty of Advanced Life Science, Hokkaido University, Sapporo 001-0021, Japan.*

Table of Contents graphic (For Table of Contents use only)

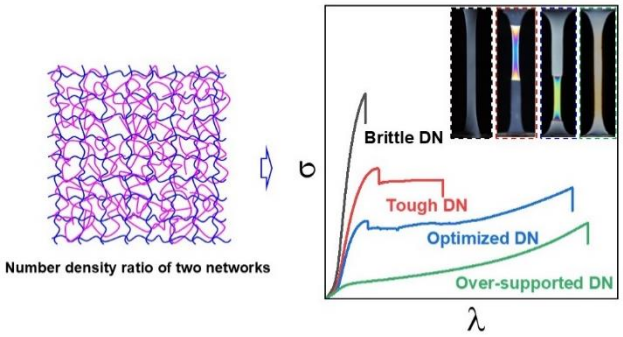

ABSTRACT

In this work, we systematically investigated how the topological and chemical structures of the first network affect the tensile behaviors of double network hydrogels. By varying the monomer type, concentration and cross-linking density of the first network while keeping the second network's structure constant, we identified four distinct categories in tensile behavior. These categories arise from changes in the topological structure of the first network, which alters the mechanical balance of the two networks, independent of the first network's chemical composition. Universal scaling relationships were observed for the strand density of the first network, including yield stress, yield stretch ratio, plateau stress, stretch ratio at strain-hardening, degree of strain-hardening, and the fracture stress. These findings suggest that ductile DN gels are defect-insensitive, with both internal and final fractures determined by their average structures. We also estimated critical number density ratios of the two network strands required for different mechanical responses. This insight allows us to predict the mechanical behavior of DN materials based on these structural averages. The established quantitative link between the topological structure of the networks and the mechanical properties of DN gels opens possibilities for customized applications.

INTRODUTION

Double network hydrogels (DN gels) are composed of two distinct networks - a highly stretched, brittle, and densely cross-linked first network, along with a condensed, flexible, and sparsely cross-linked second network. [1-3] The unique structure of DN gels imparts exceptional toughness, enabling them to demonstrate compressive fracture stresses in the range of several dozen megapascals and extraordinarily high fracture energies on the order of several $kJ \cdot m^{-2}$. [4-6] Extensive experimental and theoretical studies have demonstrated that this remarkable toughness arises from the dissipation of energy through the internal fracture of the rigid and brittle first network during the early stages of deformation. Simultaneously, the soft and highly entangled second network provides stretchability and maintains the integrity of the whole material. [7-11]

The tensile behavior of DN hydrogels is highly dependent on the intricate balance between the topological and chemical characteristics of the two networks. For typical DN gels, the unique internal fracture mechanism leads to distinct stress behaviors during uniaxial tensile tests, characterized by pronounced yielding, a plateau, and hardening with increased stretch. [12, 13] The stress-stretch ratio curve can be divided into three regions (Figures 1a and 1b). 1. Preyielding regime: The first network predominantly bears the load, and deformation is macroscopically homogeneous; 2. Necking regime: The second network predominantly supports the load due to severe breaking of the first network, and the deformation is macroscopically inhomogeneous. A narrow-necked zone coexists with the un-necked zone, and as the stretch continues

at plateau stress, the necked zone expands to the entire gauge region of the gels; 3. Hardening regime: The second network strands are extensively stretched, accompanied by the progressive fracturing of the first network into smaller "clusters", and the deformation becomes macroscopically homogeneous again.

Yielding behavior, as a crucial phenomenon in the toughening of DN gels, has been extensively investigated in numerous experimental and theoretical studies to establish a connection between network structures and yielding. [8, 14-17] Previous studies have elucidated that for a fixed first network, both the engineering yielding stress (σ_y) and stretch ratio (λ_y), when normalized to the as-prepared state, are invariant quantities solely determined by the network structure and unaffected by the preswelling state of the first network in DN gels. [8, 15] However, comprehensive and systematic studies on the relationships between other important mechanical parameters, such as plateau stress (σ_p), hardening stretch ratio (λ_h), degree of strain-hardening (k), fracture stress (σ_f), and fracture stretch ratio (λ_f), and the structures of the two networks are still lacking. Predicting these characteristic mechanical properties from the two network structures is required to tailor the DN hydrogels for specific applications, ranging from soft robotics to biomedical implants.

The structural characteristics of a network encompass both its topological structure of the network and the chemical structure of the polymer strands. The former can be tuned by monomer concentration and cross-linking density of precursor solution of the network, while the latter can be adjusted through variations in the chemical structure of monomers and their sequences. For instance, hydrophobic polyelectrolyte (hPE), a

specific subclass of polyelectrolyte (PE), are characterized by statistically distributed charged group and uncharged hydrophobic groups, exhibiting distinct properties such as hydrophilicity, charge density, and chain conformation when compared to homo-polyelectrolytes. [18-21] The study of hPE has traditionally leaned toward theoretical works due to synthetic challenges. However, our recent work successfully synthesized a series of hPE by employing ideal co-polymerization methods, providing a unique opportunity to experimentally investigate the mechanical properties of DN hydrogels with hPE serving as the first network. [22-24]

In this work, we systematically adjusted the structure of the first network, including the topological structure and the polymer chemical structure (Figure 1c), while keeping the same second network structure to fabricate DN gels. One set of positively charged polyelectrolyte (PE) networks and one set of hydrophobic polyelectrolyte (hPE) networks with varied monomer concentration and cross-linking densities were synthesized as the first network, and the correlations between the first network structures and the mechanical properties of DN gels were investigated. Specifically, we first systematically studied the shear modulus, fracture behavior, and swelling behavior of SN gels featuring different first networks (PE and hPE). Then, we explored the effect of the topological structures of the two networks on the uniaxial tensile behaviors of DN gels. We elucidated scaling relationships between the first network strands density and characteristic mechanical properties. We identified three critical number density ratios of the two network strands that result in different mechanical behaviors and internal fracture patterns of DN gels. Then we synthesized four sets of hPE networks with different polymer chemical structures as the first network to further verify the

universality of the obtained scaling relationships. Finally, we adopted a 1-D affine model to explain our observations on yielding.

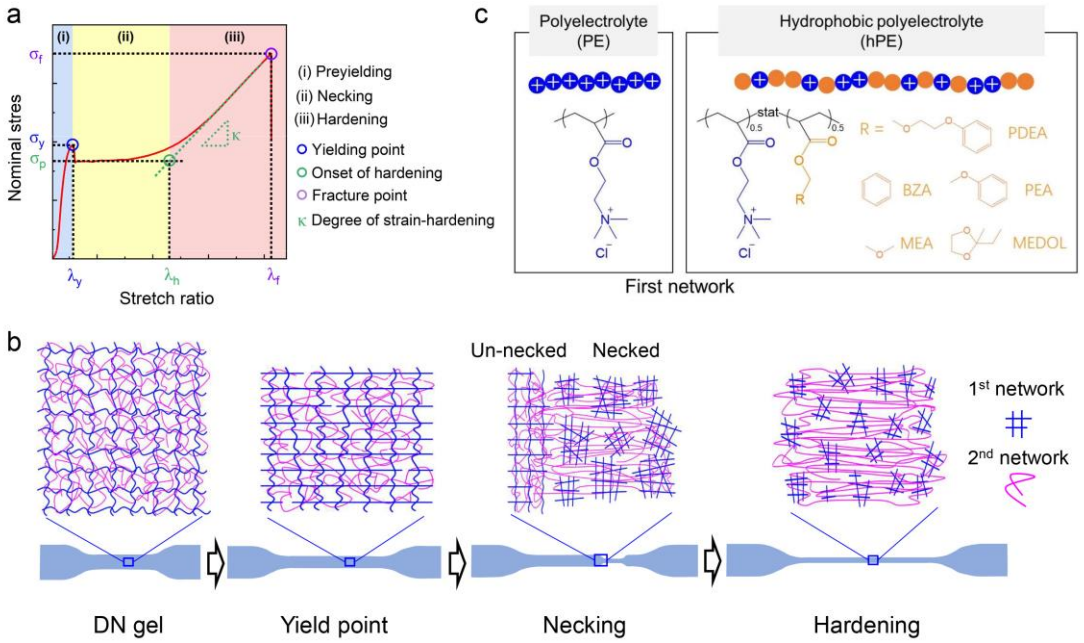

Figure 1. (a) Stress-stretch ratio curve of typical DN gel with three distinct regimes, along with the definitions of characteristic mechanical parameters. (b) Proposed internal fracture process of the first network in DN gels under stretching. (c) Chemical structures of the first network polymers. Networks of hPE are synthesized with equal molar ratio of cationic monomer and hydrophobic monomer by ideally random copolymerization.

EXPERIMENTAL SECTION

Materials. 2-(Acryloyloxy)ethyl trimethyl ammonium chloride (ATAC, 78.9% in water), 2-phenoxyethyl acrylate (PEA), benzyl acrylate (BZA), 2-(2-phenoxyethoxy)ethyl acrylate (PDEA), 2-methoxyethyl acrylate (MEA) and (2-Methyl-2-Ethyl-1,3-dioxolane-4-yl)methyl acrylate (MEDOL) were supplied by Osaka Organic Chemical Co., Ltd., Japan. Acrylamide (AAm) was purchased from Junsei Chemicals, Co., Ltd. Dimethyl sulfoxide (DMSO), *N*, *N*'-methylenebis(acrylamide) (MBAA), and 2-oxogultaric acid (α-keto) were purchased from FUJIFILM Wako Pure Chemical Corporation. All chemicals were used as received without further purification.

Synthesis of the First Network. All gels were synthesized by free radical random polymerization of monomers and cross-linkers (MBAA) with the photo-initiator (α-keto). The homo-polyelectrolyte (PE) gels were synthesized from aqueous solutions containing cationic monomer ATAC, MBAA, and α-keto. The hydrophobic polyelectrolyte (hPE) gels were synthesized from DMSO solutions containing equimolar ratio of ATAC and prescribed hydrophobic monomer, MBAA and α-keto. Two series of first network gels were synthesized. For the first series, P(ATAC) and P(ATAC-stat-PEA) single network hydrogels (SN gels) were prepared with the monomer concentration (C_m) varied in the range of 1.0 M to 1.5 M and the cross-linker concentration (Φ_x) varied in the range of 1.5 mol% to 6.0 mol% relative to C_m. This series allows us to investigate the DN gels with a wide range of topological structure. For the second series, in additional to P(ATAC) and P(ATAC-stat-PEA), four other

hPE SN gels, P(ATAC-stat-BZA), P(ATAC-stat-PDEA), P(ATAC-stat-MEA), P(ATAC-stat-MEDOL), were also prepared with the monomer concentration (C_m) of 1.5 M and the cross-linker concentration (Φ_x) varied in the range of 0.75 mol% to 2.25 mol% relative to C_m. This series allows us to investigate DN gels with different chemical structures. For both series, the initiator concentration was kept constant at 1.0 mol% relative to C_m. SN gels were synthesized by pouring the precursor solutions into glass molds of 0.5 mm-thick and irradiating them with 365 nm UV light for 8 hours in an oxygen-free glove box. For hPE SN gels, despite containing 50 mol% hydrophobic monomers, they all demonstrated transparency similar to that of P(ATAC) SN gels in water. This consistency aligns with our previous studies, affirming that the copolymerization of cationic and hydrophobic monomers in DMSO follows an ideally random process characterized by a statistical sequence. [22, 24, 25]

Synthesis of the Second Network. After the polymerization, P(ATAC) SN gels were immersed in the second monomer precursor solution for the preparation of DN gels. In the case of hPE SN gels, they were first immersed in a large amount of deionized water to remove DMSO. The water was exchanged every 6 h for over 2 days, and then the samples were placed in the aqueous second monomer precursor solution for the preparation of DN gels. The second monomer precursor solution contains 3.0 M AAm, 0.3 mM MBAA, and 0.3 mM α-keto. The SN gels were allowed to swell in the second monomer precursor solution for 1 day until reaching equilibrium. Following this, the fully swollen SN gels were sandwiched between two glass plates, transferred to an oxygen-free glove box, and irradiated with UV light from one side for 8 hours to

synthesize the DN gels. The as-prepared DN gels, ranging from 0.75 mm to 2.75 mm in thickness, were used for mechanical tests.

Linear Swelling Ratio Measurement. The as-prepared SN gels were cut into 15 mm diameter discs and allowed to reach swelling equilibrium in the second monomer precursor solution. The linear swelling ratio of SN gels (λ_s) was defined as $\lambda_s = d/d_0$, where d represents the diameter of the fully swollen gel in the second monomer precursor solution and d_0 corresponds to the diameter of as-prepared SN gel ($d_0 = 15\ mm$). The obtained λ_s stands for the linear swelling ratio of the first network in the as-prepared DN gels in relative to the as-prepared SN gel.

Uniaxial Tensile Test and Real-Time Birefringence Observation. The uniaxial tensile mechanical properties of both the as-prepared SN and DN gels were measured using a mechanical testing machine (INSTRON 5965, Instron Co.), equipped with a noncontact extensometer AVE, all conducted in an air environment at room temperature (25 °C). The test specimens were cut into the dumbbell shape standardized as IEC-540 (gauge length L_0 = 17 mm and width W_0 = 4 mm) using a gel cutting machine (Dumbbell Co., Ltd.). It is noteworthy that the sample width used in this study was larger than in previous studies[4, 8, 26] to exclude the possible sample width effect on yielding. [27] To prevent moisture loss during stretching, the sample surface was coated with paraffin. A commonly used tensile velocity (v) of 100 mm min^{-1} for highly stretchable gels was selected, corresponding to an initial strain rate of v/L_0 = 0.098 s^{-1}. The engineering stress was determined by dividing the tensile force by the initial cross-

section area of the sample gauge. For calculating the stretch ratio, two white dots were initially marked within the sample gauge region. In the early stages of a uniaxial tensile test before reaching the yield point, the gels predominantly experienced macroscopic uniform deformation. Consequently, the stretch ratio was computed by dividing the distance between these two dots after stretching by the initial distance between them, as measured using the non-contact extensometer. Beyond the yield point, the materials underwent macroscopic non-uniform deformation, manifesting both necking and non-necking regions. In this deformation regime, the stretch ratio was determined by dividing the displacement of crosshead by the initial gauge length. At least three measurements were performed for each sample, and the error bars on each data point represent their respective standard deviations.

To conduct real-time birefringence observations during the tensile test, we used the same experimental setup as described in the literature. [5, 28] The sample was placed between two crossed circular polarizing films. One polarizing film was positioned in front of a white light lamp, and another was placed in front of a recording camera. Birefringence images were recorded in real-time during the uniaxial stretching process using a video camera (24 frames/s, 1920×1080 pixels, Sony α7S E-mount camera, Sony Electronics Inc.), in a darkroom.

RESULTS AND DISCUSSION

1. Effect of Topological Structures of the First Network on DN Gels.

1.1 First Network

Network structures of SN gels. First, we studied P(ATAC) and P(ATAC-stat-PEA) systems as representative examples for PE and hPE gels. The nominal stress-stretch ratio curves of the as-prepared SN gels are depicted in Figure 2. To delve into the network structure, we estimated the shear modulus (G_0) from the Mooney-Rivlin plots [29] (Figure S1), with the results shown in Figures 3a and 3b. Notably, we observed that G_0 increases with increasing Φ_x(Figure 3a) and C_m (Figure 3b) for both P(ATAC) and P(ATAC-stat-PEA) SN gels. Most of P(ATAC-stat-PEA) SN gels exhibited slightly higher G_0 values than P(ATAC) SN gels at the same Φ_x and C_m, suggesting that the introduction of hydrophobic monomers and changes in the solvent of synthesis led to minor increases in the strand density. We calculated the number density of elastically effective network strands ($\nu_{e,0}$, Figures 3a, b) using the classical phantom network model, [29, 30] as expressed by the equation

$$G_0 = \left(1 - \frac{2}{f}\right)\nu_{e,0}k_BT \quad (1)$$

where k_B is Boltzmann's constant, T is the absolute temperature, and $f = 4$ is the functionality of the cross-linker. For an ideal cross-linking reaction with $f = 4$, the network strands density is $2C_m\Phi_x$. Thus, the ratio of $\nu_{e,0}$ to $2C_m\Phi_x$ represents the efficiency of cross-linking reaction in forming elastically effective strands. From Figure 3a, the efficiency was estimated to range from 5% to 28%, with slightly higher values

observed in P(ATAC-stat-PEA) SN gel. The efficiency increased with C_m and showed a slight increase with Φ_x (Figure S2) in both SN gels. Several reasons account for the low efficiency, including the formation of ineffective elastic network strands, such as loops and dangling chains, [31] the deactivation of double bonds in cross-linkers by the attack of excessive initiators, [31] and the presence of unreacted double bonds in the network. [32]

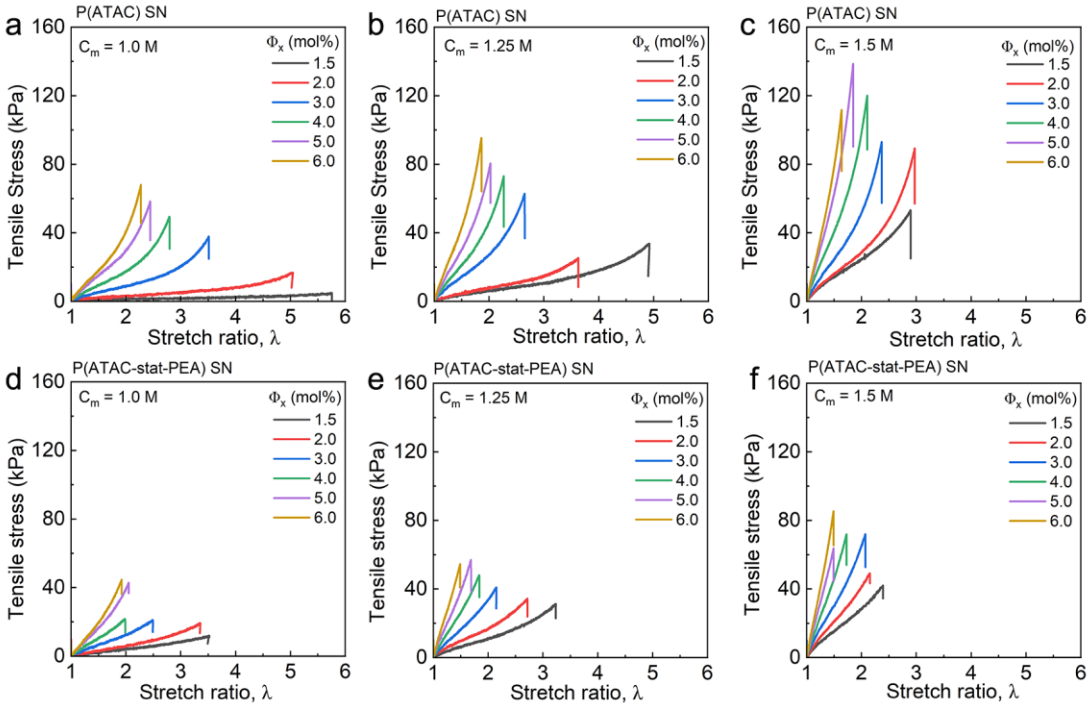

Figure 2. Effect of monomer concentration (C_m) and cross-linker density (Φ_x) on the stress-stretch ratio curves of as-prepared P(ATAC) and P(ATAC-stat-PEA) SN gels. (a-c) P(ATAC) SN gels with various Φ_x at different C_m. (d-f) P(ATAC-stat-PEA) SN gels with various Φ_x at different C_m.

Further analysis of the fracture behaviors revealed that both types of SN gels demonstrated an increase in fracture stress ($\sigma_{SN,f}$) (Figure 3c) and a decrease in fracture stretch ratio ($\lambda_{SN,f}$) (Figure 3d) with increasing $\nu_{e,0}$ (or Φ_x). We noticed that P(ATAC) SN gels exhibited higher fracture stress and stretch ratios than P(ATAC-stat-PEA) SN gels at the same $\nu_{e,0}$. The fracture behavior of SN gels is known to be highly susceptible to defects. [33-35] The observed differences in fracture behavior between P(ATAC) and P(ATAC-stat-PEA) SN gels could be attributed to internal or surface defects. P(ATAC-stat-PEA) SN gels synthesized in DMSO might possess more internal defects than P(ATAC) gels synthesized in water, as the organic solvent has a higher chain transfer constant than water during free radical polymerization. [36, 37] Moreover, we observed that the surface of P(ATAC-stat-PEA) SN gels exhibits stickiness to the metal cutter used for sample preparation, which might introduce surface defects.

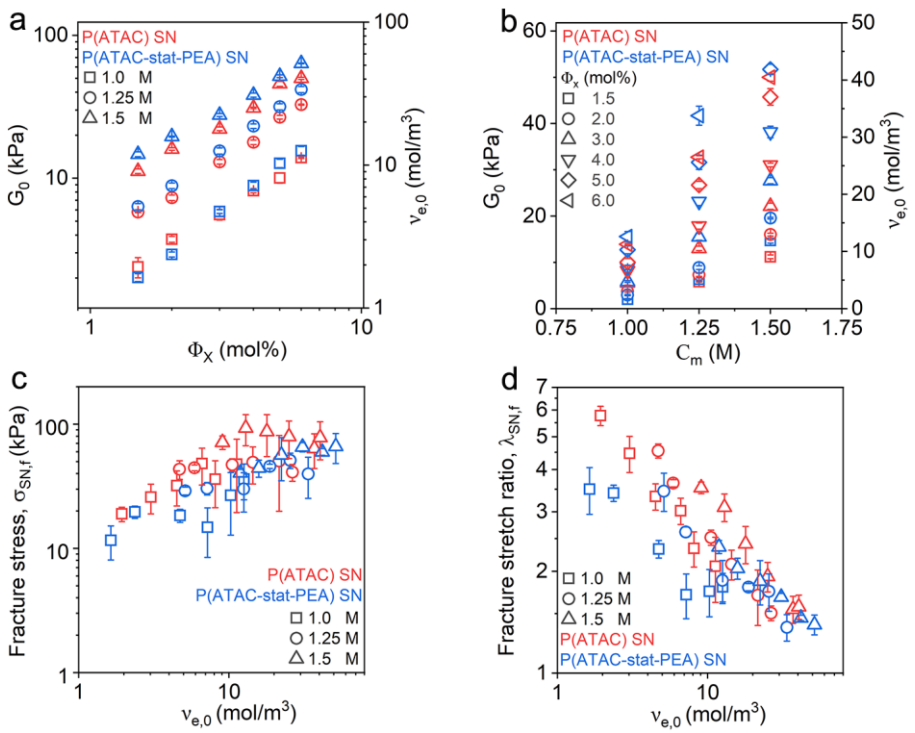

Figure 3. Behaviors of P(ATAC) and P(ATAC-stat-PEA) single network hydrogels prepared at various formulations. (a, b) Dependences of shear modulus G_0 and number density of elastically effective strands $\nu_{e,0}$ of the as-prepared SN gels on Φ_x (a) and C_m (b). (c, d) Dependences of fracture stress ($\sigma_{SN,f}$) (c) and fracture stretch ratio ($\lambda_{SN,f}$) (d) on $\nu_{e,0}$. The red and blue points represent the data for P(ATAC) SN gels and P(ATAC-stat-PEA) SN gels, respectively. The error bars are standard deviations of $n = 3$ measurements.

Swelling behavior of SN gels. We next measured the linear swelling ratio of SN gels. Both types of SN gels displayed significant swelling when immersed in the second network precursor solution. As illustrated in Figure 4a, the linear swelling ratios (λ_s) exhibited a significant decrease with increasing Φ_x and C_m. Specifically, P(ATAC)

SN gels exhibited larger swelling ratios compared to P(ATAC-stat-PEA) SN gels, potentially influenced by either the topological structure or the hydrophilicity of the networks. We further plotted the linear swelling ratio (λ_s) against the strand density at the as-prepared state ($\nu_{e,0}$) (Figure 4b). Roughly, they obey a scaling relationship of $\lambda_s \propto {\nu_{e,0}}^{-0.4}$. The scaling relation of $\lambda_s \propto {\nu_{e,0}}^{-0.4}$ tells that each network strand is in a highly extended state, which will be discussed in section 3.

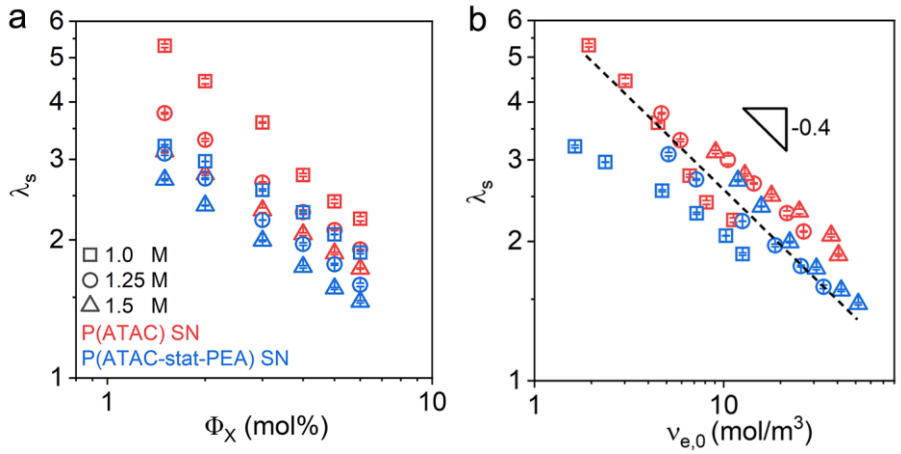

Figure 4. (a, b) Dependences of linear swelling ratio (λ_s) of SN gels on Φ_x (a) and $\nu_{e,0}$ (b). Both figures have the same legend. The red and blue points represent the data for P(ATAC) SN gels and P(ATAC-stat-PEA) SN gels, respectively. The black dashed line in (b) is a guide to the eyes. The error bars are standard deviations of $n = 3$ measurements.

1.2 Double network

Tensile behaviors of DN gels. Next, we conducted uniaxial tensile tests on the as-prepared P(ATAC) and P(ATAC-stat-PEA) DN gels to examine the impact of the first

network structure on their mechanical properties (Figure 5). With increasing C_m and Φ_x, which correspond to an increase in the strand density of the first network in DN gels, $\nu_{e,1} = \nu_{e,0}/{\lambda_s}^3$, we identified four distinct categories of tensile behavior as shown in Figure 5d. Since the strand density of the second network ($\nu_{e,2}$) in these DN gels is constant, changes in $\nu_{e,1}$ alter the strength balance between the two networks, with an increase in the first network strand density resulting in a relative weakening of the second network. Based on their tensile behavior with increasing $\nu_{e,1}$, we classify these DN gels as over-supported DN, optimized DN, tough DN, and brittle DN. At low $\nu_{e,1}$, the stress continuously increases with stretching, and the samples undergo nearly uniform deformation until fracture, with widespread damage observed in the first network (over-supported DN, Figure S3a, Video S1). As $\nu_{e,1}$ increases, the stress-stretch curves begin to exhibit typical DN behavior as shown in Figure 1a, including yielding, necking, and strain-hardening before fracture (optimized DN, Figure S3b, Video S2). Hardening occurs when the necking zone, which indicates significant damage in the first network, expands to the entire gauge length of the sample. As $\nu_{e,1}$ further increases, fracture occurs within the necking regime, before reaching the hardening regime (tough DN, Figure S3c, Video S3). At very high $\nu_{e,1}$, both hardening and necking diminish, and fracture occurs in the preyielding regime (brittle DN, Figure S3d, Video S4), indicating a transition from toughness to brittleness.

Next, we analyze the effects of topological and chemical structures on these characteristic mechanical behaviors. We extract characteristic mechanical parameters, including yielding stress (σ_y), yielding stretch ratio (λ_y), plateau stress (σ_p), hardening

stretch ratio (λ_h), fracture stress (σ_f), and fracture stretch ratio (λ_f), from the stress-stretch curves to elucidate their correlations with $\nu_{e,1}$ in the DN gels. The correlations of these parameters with the in-feed monomer concentration (C_m) and cross-linker density (Φ_x) are summarized in Figure S4.

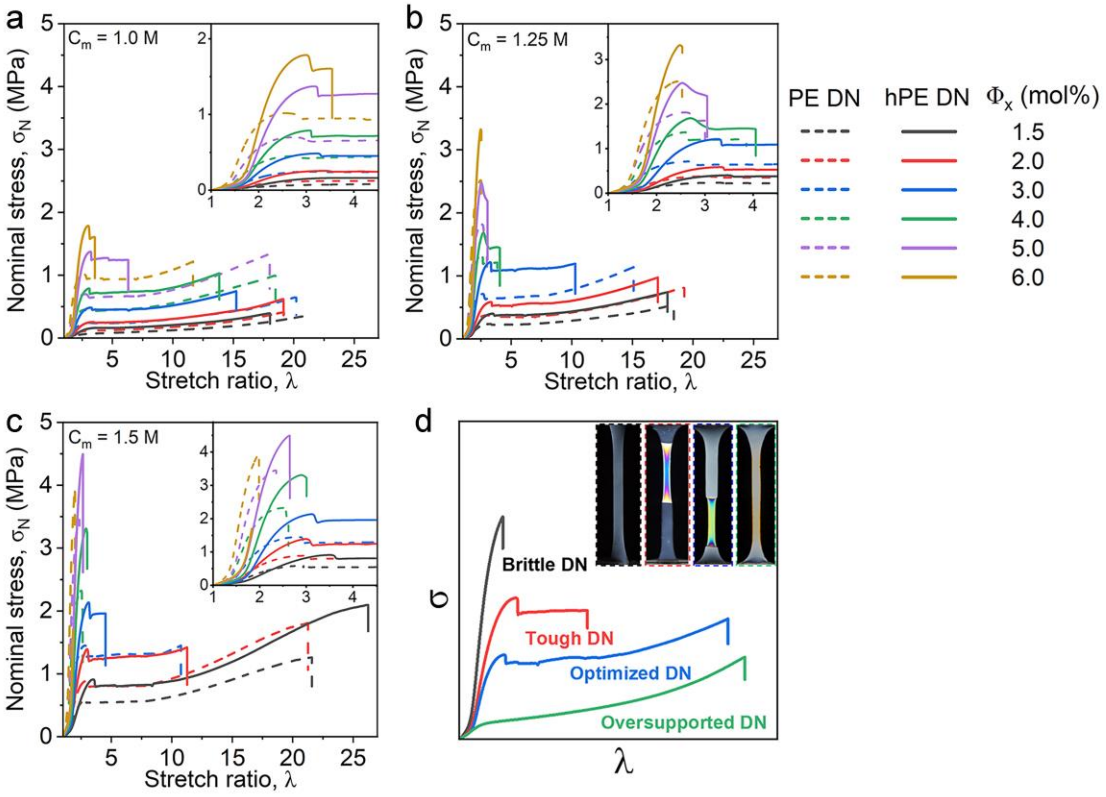

Figure 5. (a-c) Tensile stress-stretch ratio curves of P(ATAC) DN gels (PE DN, dashed curves) and P(ATAC-stat-PEA) DN gels (hPE DN, solid curves) with varying monomer concentration (C_m) and cross-linker density (Φ_x) in the first network, while keeping the same formulation of the second network. (d) Four distinct categories of tensile behavior and corresponding birefringence images during stretching (from left to right: Brittle, Tough, Optimized, Over-supported, details are shown in Figure S3, SI).

The measurements were performed on the as-prepared DN gels. Figures (a-c) have the same legend.

Yielding stress and stretch ratio. The optimized DN and tough DN exhibit yielding and necking. Here we define the yield point as the point at which the local slope of the stress-stretch ratio curve becomes zero, marking the transition from the preyielding regime to the necking regime (Figure 1a). In the preyielding regime, the load is predominantly borne by the first network. Accordingly, we examined how the engineering yielding stress (σ_y), yielding stretch ratio (λ_y), and true yielding stress ($\sigma_{T,y} \equiv \sigma_y \lambda_y$) vary with the strand density of the first network ($\nu_{e,1}$) in the DN gels, as detailed in Figure 6. Notably, although the dependence of linear swelling ratio (λ_s) on the strand density of as-prepared first network ($\nu_{e,0}$) changed for the two sets of first networks (Figure 4b), the data points in Figure 6 showed significant overlap, indicating that the mechanical properties in this regime are governed by the strand density of the first network, regardless of its chemical structure. Specifically, it was observed that an increase in strand density leads to higher engineering stress, following the scaling relationships $\sigma_y \propto {\nu_{e,1}}^{0.59}$ (Figure 6a), while the yield stretch ratio exhibited a slightly decreasing trend with increasing strand density, $\lambda_y \propto {\nu_{e,1}}^{-0.09}$ (Figure 6b), consistent with our previous observations. [26] As a result, the true yield stress $\sigma_{T,y} \propto {\nu_{e,1}}^{0.49}$ (Figure 6c).

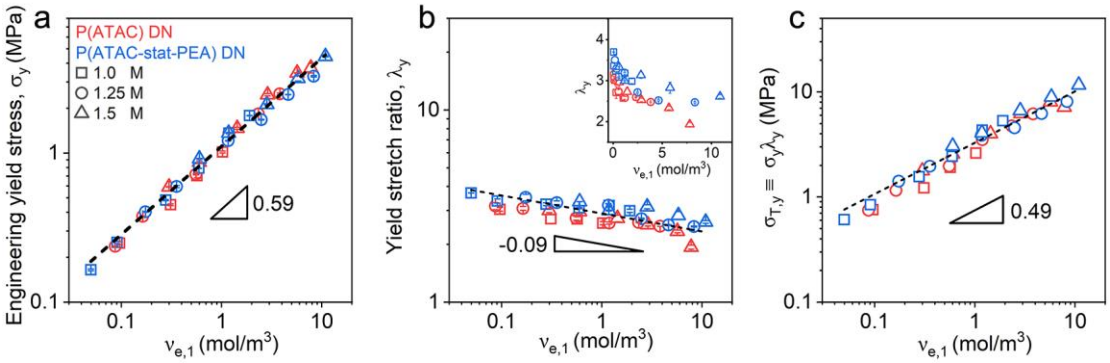

Figure 6. Yielding behaviors of DN gels. (a-c) Dependences of engineering yield stress (a), yield stretch ratio (b), and true yield stress (c) on the number density of elastically effective strands of the first network ($\nu_{e,1} = \nu_{e,0}/{\lambda_s}^3$) in DN gels. An inset linear plot is included in (b) to highlight the details of the decreasing trend. All figures have the same legend. The red points and blue points represent the data for P(ATAC) DN gels and P(ATAC-stat-PEA) DN gels, respectively. All the black dashed lines represent the power-law fitting.

Our previous studies revealed that the yield stress and stretch ratio scale with the swelling ratio of the first network as $\sigma_y \sim {\lambda_s}^{-2}$ and $\lambda_y \sim {\lambda_s}^{-1}$, respectively. [8, 15] These findings suggest that the yielding point remains invariant with respect to the swelling ratio (λ_s) of the first network when normalized to its as-prepared state (reference state). This outcome mitigates the influence of swelling and facilitates the comparison of DN gels with different chemistries of the first network by utilizing normalized yield stress ($\sigma_Y \equiv \sigma_y {\lambda_s}^2$) and stretch ratio ($\lambda_Y \equiv \lambda_y \lambda_s$), where σ_Y and λ_Y represent the engineering yield stress and yield stretch ratio, respectively, of the DN gels normalized

to the as-prepared first network. The logarithmic plots in Figures 7a and 7b depict σ_Y and λ_Y as functions of the strand density of as-prepared first network ($\nu_{e,0}$), respectively. Despite variations in the monomer concentration and the broad range of cross-linker concentration of the first network, all data points of σ_Y and λ_Y, except for the two data points with a strand density below 3 mol/m^3, roughly fell on the straight lines (The large deviation of data points at low concentrations will be discussed in section 3). These observations indicate that the yielding point depends solely on the topological structure of the first network, independent of their chemistries. From the slopes of the straight lines, universal scaling relationships are observed:

$$\sigma_Y \propto {\nu_{e,0}}^{0.5} \tag{2}$$

$$\lambda_Y \propto {\nu_{e,0}}^{-0.5} \tag{3}$$

These two scaling relationships lead to the result that the true yielding stress $\sigma_{T,Y}$, which is the product $\sigma_Y\lambda_Y$, is roughly a constant, independent of $\nu_{e,0}$ for both DN gels, as depicted in Figure 7c. Furthermore, we observed that $\sigma_{T,Y}$ increases with the first network monomer concentration at preparation C_m (Figure 7d), as

$$\sigma_{T,Y} \propto {\nu_{e,0}}^0 C_m \tag{4}$$

Equation 4 indicates that the true yielding stress normalized to the as-prepared state of the first network is independent of its cross-linking density but increases as the polymer density increases. This result is consistent with our previous observation on DN gels composed of polyanion as the first network. [8] These findings in yielding will be elaborated upon in detail from a polymer chain perspective in section 3.

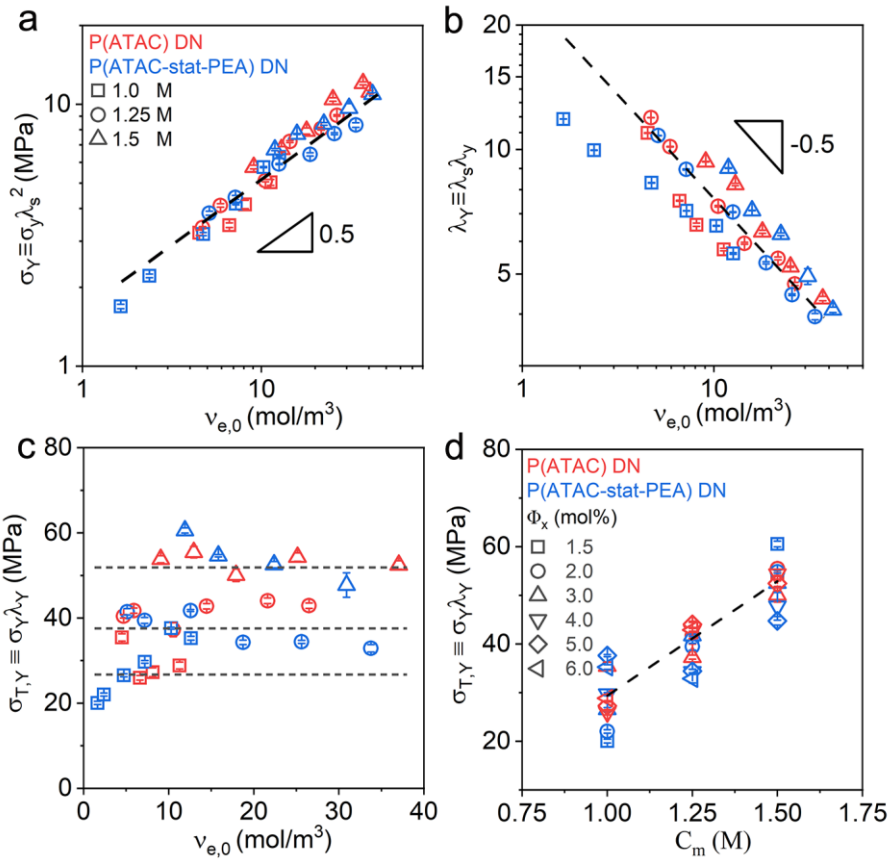

Figure 7. (a, b) Normalized yield stress σ_Y ($\sigma_Y \equiv \sigma_y {\lambda_s}^2$) (a) and stretch ratio λ_Y ($\lambda_Y \equiv \lambda_s \lambda_y$) (b) with respective to the as-prepared first network as a function of the strand density of the as-prepared first network $\nu_{e,0}$. (c, d) Normalized true yield stress $\sigma_{T,Y}$ ($\sigma_{T,Y} \equiv \sigma_Y \lambda_Y$) as functions of $\nu_{e,0}$ (c) and monomer concentration C_m (d) of as-prepared first network. The red points and blue points represent the data for P(ATAC) DN gels and P(ATAC-stat-PEA) DN gels, respectively. Figures (a-c) have the same legend. All the black dashed lines are a guide to the eyes.

Plateau stress and necking. For DN gels that exhibit yielding and necking phenomenon, beyond the yielding point, the stress shows a plateau after an abrupt stress

drop, and the stress drop becomes distinct for DN gels with large $\nu_{e,1}$ (Figure 5). The plateau stress (σ_p) as a function of the number density of the first network strands ($\nu_{e,1}$) in DN gels is shown in Figure 8a. Again, the data points of all the gels exhibited significant overlap, indicating that mechanical behaviors depend primarily on the topological structure, independent of the chemical structure of the network polymers. The plateau stress increases as the strand density ($\nu_{e,1}$) increases, following a scaling relationship as

$$\sigma_p \propto {\nu_{e,1}}^{0.57} \tag{5}$$

This scaling exponent is comparable to the one identified for the engineering yield stress (Figure 6a). Thus, with a fixed second network, the plateau stress increases with the strand density of the first network. This can be understood by considering the coexistence of un-necked region, where the load is predominately borne by the first network, and the necked region, where the load is predominately borne by the second network. The plateau stress is required to break the first network in the un-necked region, so it increases with $\nu_{e,1}$. To mitigate the influence of swelling and facilitates the comparison of DN gels with different first network, the plateau stress normalized to the as-prepared first network $\sigma_P \equiv \sigma_p {\lambda_s}^2$ is derived as $\sigma_P \propto {\nu_{e,0}}^{0.45}$.

We noticed that the plateau stress (σ_p) was slightly lower than the yield stress (σ_y) at high values of $\nu_{e,1}$. Figure 8b depicts $\frac{\sigma_p}{\sigma_y}$ as a function of $\nu_{e,1}$. Here, we roughly defined the ratio of plateau stress to yield stress as 1 for over-supported DN gels, as shown in the curve in Figure S3a. We observed that the ratio $\frac{\sigma_p}{\sigma_y}$ decreases as $\nu_{e,1}$ increases for DN gels with a distinct yield point that fractured in the hardening regime

(pink region in Figure 8b), and reaches to a constant for DN gels fractured in the necking regime (yellow region in Figure 8b), indicating a more pronounced difference at large $\nu_{e,1}$. The difference between σ_p and σ_y should arise from modulus difference of the two networks, which increases with $\nu_{e,1}$ in the present case. For a higher plateau stress σ_p, the second network should be stretched more in necking regime. To confirm this, we determined the tensile stretch ratios in each region. Because it is difficult to measure the tensile stretch ratios in each region directly, we measured the shrinking ratios in the lateral direction (width direction) of these two regions by using a birefringence observation set up.[28] We adopted P(ATAC-stat-PEA) DN gels as representative, and measured width in necked (W_n) and un-necked (W_{un}) regions at a global stretching ratio of 5-6, at which the necked and un-necked zones coexisted (Figure 8c). The stronger birefringence in the necked zone compared to the un-necked zone indicates that the second network strands are more highly oriented along the stretch direction, bearing the load in the necked zone.

As shown in Figure 8d, the lateral shrinking ratio in the necked region ($\lambda_{n,\perp} = \frac{W_n}{W_0}$, where $W_0 = 4\ mm$ is the initial width before stretching) decreases rapidly as $\nu_{e,1}$ increases in the regime that fracture occurs at hardening and then reaches a plateau as $\nu_{e,1}$ reaches the regime that the fracture occurs at necking. The lateral shrinking ratio in un-necked region ($\lambda_{un,\perp} = \frac{W_{un}}{W_0}$) slightly increases as $\nu_{e,1}$ increases over the whole observation range. As a result, the ratio of lateral shrinking ratio in these two regions ($\frac{\lambda_{n,\perp}}{\lambda_{un,\perp}}$) decreases rapidly as $\nu_{e,1}$ increases when fracture occurs at hardening and is almost independent of $\nu_{e,1}$ when the fracture occurs at necking (Figure 8e). According

to the incompressible condition of gels, the ratio of tensile stretch ratio in the two regions $\frac{\lambda_n}{\lambda_{un}}$ can be estimated through the relationship of $\frac{\lambda_n}{\lambda_{un}} = \left(\frac{\lambda_{n,\perp}}{\lambda_{un,\perp}}\right)^{-2}$. Therefore, $\frac{\lambda_n}{\lambda_{un}}$ exhibit a similar increasing trend as $\nu_{e,1}$ increases (Figure 8e), indicating more pronounced difference in the stiffness of necked and un-necked regions.

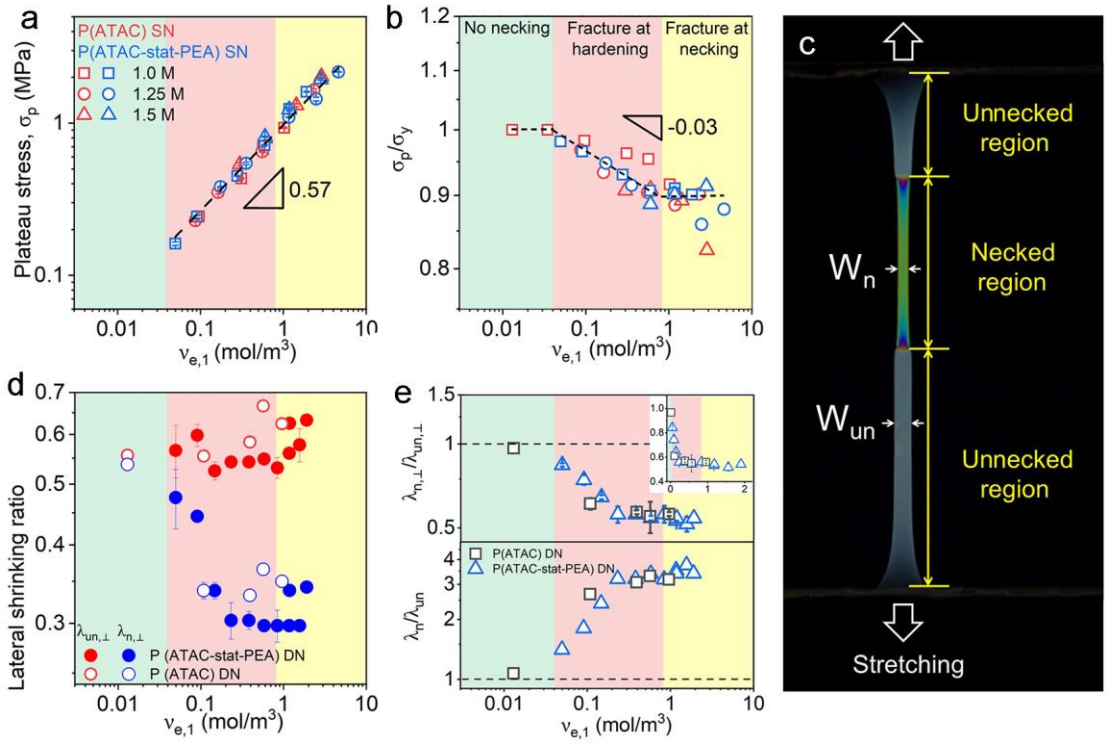

Figure 8. Birefringence observation and necking behavior of DN gels. (a, b) Dependences of plateau stress (σ_p) (a), and ratio of plateau to yielding stresses ($\frac{\sigma_p}{\sigma_y}$) (b) on the number density of elastically effective strands of the first network ($\nu_{e,1} = \frac{\nu_{e,0}}{\lambda_s^3}$) in DN gels. (c) Birefringence image of a sample under stretching to the necking regime and the definition of widths for necked and un-necked regions. (d, e) Lateral shrinking ratios in un-necked ($\lambda_{un,\perp}$) and necked ($\lambda_{n,\perp}$) regions (c), and their ratio ($\frac{\lambda_{n,\perp}}{\lambda_{un,\perp}}$) and the tensile deformation ratio in the two regions $\frac{\lambda_n}{\lambda_{un}} = \left(\frac{\lambda_{n,\perp}}{\lambda_{un,\perp}}\right)^{-2}$ (d) as functions of $\nu_{e,1}$. An inset linear plot is included in (e). The dashed line in (a) presents the power-law

fitting. The dashed lines in (b, e) are a guide to the eyes. The green, pink, and yellow colors present over-supported DN, optimized DN, tough DN gels, respectively.

The behavior of $\frac{\sigma_p}{\sigma_y}$ at various $\nu_{e,1}$ reveals different internal fracture process of the first network as the relative strength of the two networks changes. The overshoot of yield stress in necking DN gels (optimized DN and tough DN) is related to the energy barrier associated with the initiation of cracks in the first network, which leads to auto-accelerated crack propagation. [27] In un-necking DN gels (over-supported DN), the first network strands break randomly in space without developing into auto-accelerated crack propagation, resulting in the absence of a stress overshoot. To confirm this explanation, we conducted uniaxial tensile tests and birefringence observations on DN gels with a pre-damaged line along the width, ensuring that the first network already contained a crack. The pre-damage of the first network was introduced by compressing the sample with a hard indent, 1.1 mm thick. We performed the experiments on optimized P(ATAC) DN gels ($\nu_{e,1} = 0.57\ mol/m^3$, Video S5). We observed that the stress overshoot at the yield point disappeared in the pre-damaged sample, and necking expanded from the pre-damaged position (Figure 9a, Video S6). In contrast, for over-supported P(ATAC) DN gels ($\nu_{e,1} = 0.013\ mol/m^3$, Video S7), the pre-damage did not influence the deformation behavior and the stress -stretch ratio curve (Figures 9b, Video S8). These observations are consistent with our explanation that the stress

overshoot at the yield point in necking samples is related to the energy barrier for crack initiation in the first network of the DN gels.

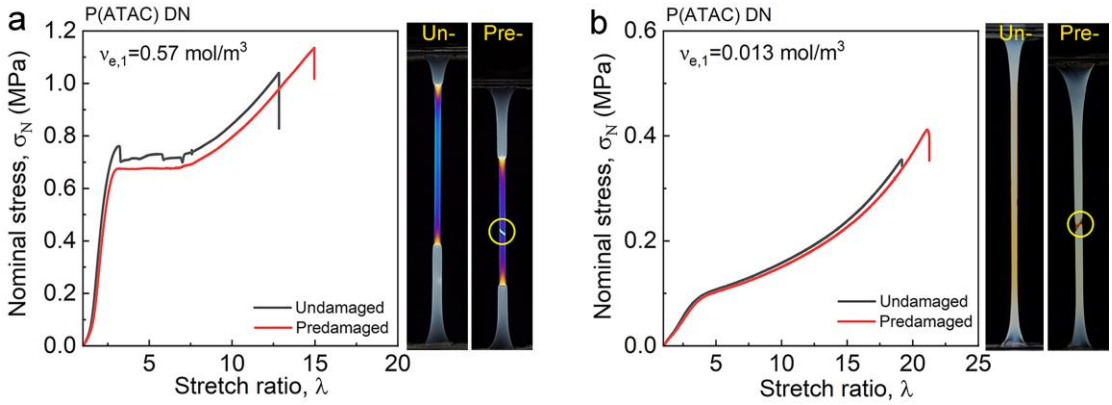

Figure 9. (a, b) Tensile stress-stretch ratio curves and birefringence images of P(ATAC) DN gels with and without a pre-damage along the sample width direction under uniaxial stretching at necking regime. The yellow rings in birefringence images represent the location of pre-damage.

Hardening and Fracture. The hardening stretch ratio (λ_h) corresponds to the point where the necking zone has developed to the entire sample, and the second network predominantly bears the load throughout the entire sample. We observed from the stress-stretch ratio curve that λ_h exhibits a slightly increasing trend as $\nu_{e,1}$ increases (Figure 10a). This trend is consistent with the behavior of the lateral shrinking ratio of necked region ($\lambda_{n,\perp}$) (Figure 8d), which correlates with λ_h through the incompressibility condition of gels as $\lambda_h \approx (1/\lambda_{n,\perp})^2$. The increasing trend of λ_h

with $\nu_{e,1}$ is because the stress required to expand the necking zone σ_p increases as $\nu_{e,1}$ increases. Consequently, the second network, which mainly bears the load in the necked region, requires a higher stretch ratio. The observed range of 5 to 10 for λ_h is much smaller than the fracture stretch ratio (~20) of the PAAm SN gel (Figure S1g). Therefore, as strain-hardening occurs when the entire sample reaches necking, the hidden length of the second network is not fully released, indicating that the first network still carries load. Previous studies assumed that in the necking region, the brittle first network has fractured into fragments, which entangle with the second network and restrict the deformation of the second network to a certain extent. These fragments act similarly to slidable cross-linking points in the second network, enhancing the force transmission. [13, 38 39]

To delve deeper into this phenomenon on, we computed the strain-hardening degree ($\kappa \equiv \frac{\Delta\sigma}{\Delta\lambda}$, Figure 1a) from the stress-stretch ratio curves that exhibit a linear trend in the stretch ratio ranging from 12 to 20. Despite the possible errors in determining the stretch ratio, the strain-hardening degree for DN gels with various chemistries are largely overlapped, following a scaling relationship $\kappa \propto {\nu_{e,1}}^{0.59}$ (Figure 10b). Furthermore, we found that the fracture stress (σ_f) increases as $\nu_{e,1}$ increases, adhering to the scaling relationship $\sigma_f \propto {\nu_{e,1}}^{0.44}$ (Figure 10c). Previous studies have demonstrated that in the strain-hardening regime, the first network continues to break, dissipating energy. [13, 26] The dependence of the strain-hardening degree and fracture stress on the first network clearly indicates that the first network "clusters" continue to carry the load

in this regime. A higher $\nu_{e,1}$ can bear higher stress, leading to an increased strain-hardening degree and fracture stress.

The fracture stretch ratio (λ_f) remains constant, aligning well with the fracture stretch ratio (~20) of the PAAm SN gel, regardless of $\nu_{e,1}$ for fractures occurring in hardening regime. However, it decreases as $\nu_{e,1}$ increases for fractures occurring in the necking regime. Given that the 1st network clusters carry load up to the fracture point, the similar fracture stretch ratio (~20) of both DN and PAAm suggests that the PAAm SN gel does not reach full extension at fracture. This is reasonable, considering that a SN is flaw-sensitive. These results indicates that when the second network strength is relatively high, it can bear the load up to straining-hardening regime, during which, the first network fragments gradually fracture into small "clusters" through force transmission from the second network. However, when the second network is relatively weak, it breaks before breaking the first network clusters.

The boundaries for four categories of DN gels. The shape of the stress-stretch ratio curves for DN gels is determined by the strength balance between the two networks. As the strand density of the first network ($\nu_{e,1}$) increases, the relative strength of the second network decreases. We calculated the elastically effective strand density for the second network ($\nu_{e,2} = 17.9\ \mathrm{mol \cdot m^{-3}}$, Figures S1h and S5a). Figures 10e and 10f show the fracture stress (σ_f) and fracture stretch ratio (λ_f), relative to the yielding stress (σ_y) and yielding stretch ratio (λ_y), respectively, as functions of $\nu_{e,1}$ (lower horizontal axis) and $\frac{\nu_{e,2}}{\nu_{e,1}}$ (upper horizontal axis). Yield stress and yield stretch ratio values from

the fitted curves in Figures 7a and 7b were for over-supported and brittle DN gels. Our analysis identified three boundary values of $\frac{\nu_{e,2}}{\nu_{e,1}}$, which define the four categories of DN gels:

1. **Over-supported DN Gels** ($\frac{\lambda_f}{\lambda_y} > 1$ and $\frac{\sigma_f}{\sigma_y} > 1$) appear when $\frac{\nu_{e,2}}{\nu_{e,1}}$ > 400 (green region). In this regime, the second network is so strong that it prevents the first network from fracturing to the percolation threshold, eliminating necking.

2. **Optimized DN Gels** (typical DN gels) that fracture in the hardening regime ($\frac{\lambda_f}{\lambda_y} > 1$ and $\frac{\sigma_f}{\sigma_y} > 1$) are seen when $21 < \frac{\nu_{e,2}}{\nu_{e,1}} < 400$ (pink region). Here, the second network is soft but strong enough to sustain the load after the percolative fracture of the first network to show strain-hardening.

3. **Tough DN Gels** that fracture in the necking regime ($\frac{\lambda_f}{\lambda_y} > 1$ but $\frac{\sigma_f}{\sigma_y} \simeq 1$) appear when $1.5{\sim}4.8 < \frac{\nu_{e,2}}{\nu_{e,1}} < 21$ (yellow region). In this range, the second network is barely strong enough to sustain load after the percolative fracture of the first network, resulting in necking but not sustaining strain-hardening.

4. **Brittle DN Gels** that fracture before yielding ($\frac{\lambda_f}{\lambda_y} < 1$ and $\frac{\sigma_f}{\sigma_y} < 1$) occur when $\frac{\nu_{e,2}}{\nu_{e,1}} > 1.5{\sim}4.8$ (blue region). In these gels, the second network's strength is insufficient to support the material when the first network has localized damage, leading to fracture before yielding.

These boundary values appear independent of the first network's chemical structure, except for that of tough - brittle transition. P(ATAC-stat-PEA) DN gels

exhibit a lower $\frac{\nu_{e,2}}{\nu_{e,1}}$ threshold (~1.5) for this transition compared to P(ATAC) DN gels (~4.8). This difference aligns with the relatively weaker first network in P(ATAC-stat-PEA) SN gels, which show lower fracture stress and stretch ratios than P(ATAC) SN gels at equivalent strand densities (Figures 3c, d). These findings, together with the universal scaling relations for mechanical parameters of yielding, necking, strain-hardening, and final fracture indicates that for the ductile DN gels, including over-supported, optimized, and tough DN gels, are defect-insensitive, and the internal fracture and final fracture are determined by their average structures. However, brittle DN gels are defect sensitive and their fracture is determined by casually induced defects. It is important to note that the observed boundary values of $\frac{\nu_{e,2}}{\nu_{e,1}}$ apply to a fixed strand length of the second network. Variations in the extensibility of the second network would alter these boundary values.

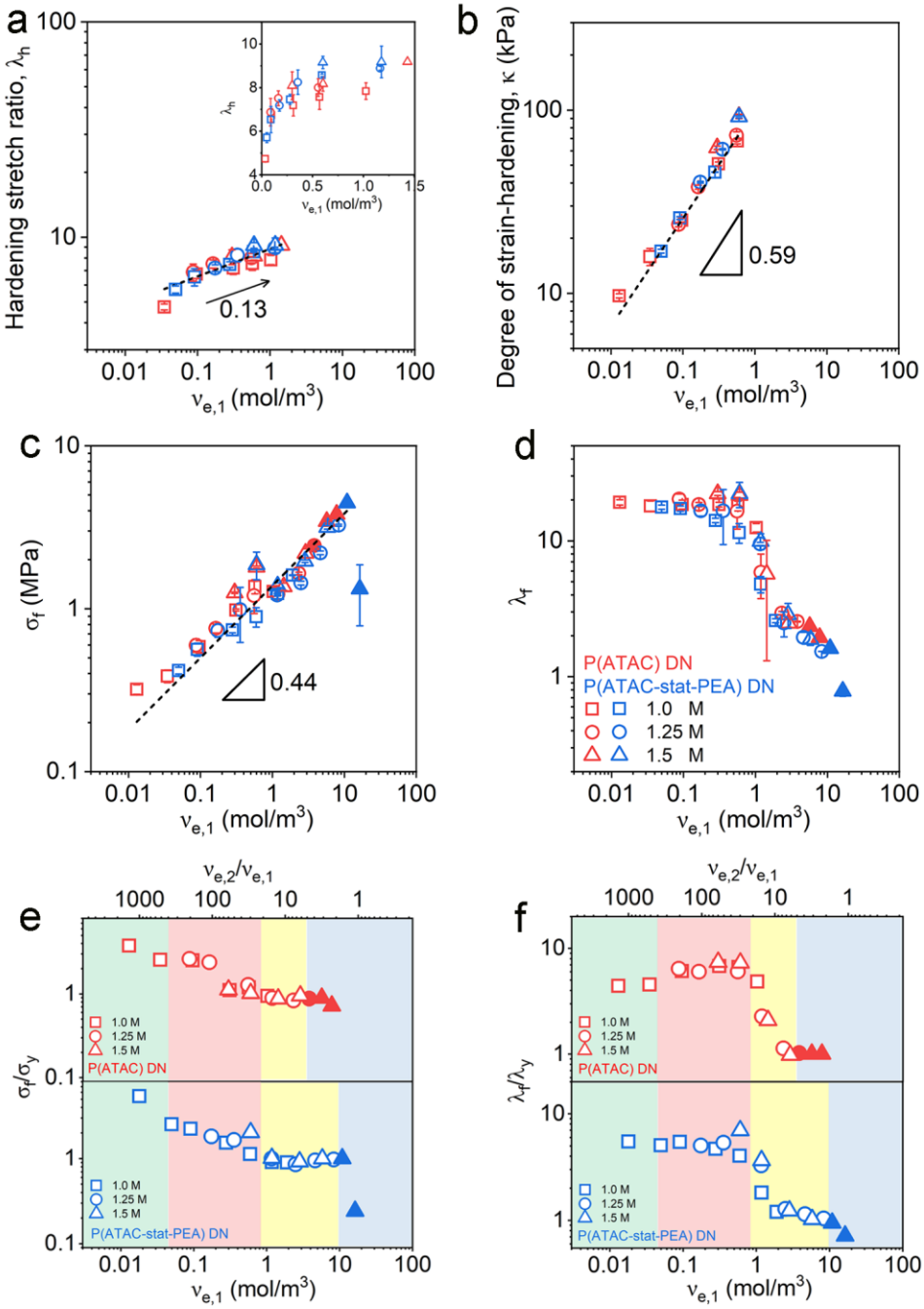

Figure 10. Characteristic mechanical parameters extracted from the stress-stretch ratio curves of D gels. (a-f) Dependences of hardening stretch ratio (λ_h) (a), degree of strain-hardening (κ) (b), fracture stress (σ_f) (c), fracture stretch ratio (λ_f) (d), $\frac{\sigma_f}{\sigma_y}$ (e), and $\frac{\lambda_f}{\lambda_y}$ (f) on the number density of elastically effective strands of the first network ($\nu_{e,1}$) in DN gels. An inset linear plot is included in (a). The dashed lines in (a-c) present the power-law fitting. The ratios of $\nu_{e,2}/\nu_{e,1}$ are also showed in (e, f). In Figures (a-f), the

red and blue data points represent the data for P(ATAC) DN gels and P(ATAC-stat-PEA) DN gels, respectively. In Figures (c-f), open data dots denote ductile DN gels characterized by a well-defined yield point, whereas solid data dots correspond to brittle gels that fracture at a low stretch ratio without exhibiting a yield point, the theoretical yield stress and yield stretch ratio were estimated from the fitted curves in Figures 7 (a, b). The green and pink regions in (e, f) present over-supported and optimized DN gels fracturing in the hardening regimes without and with necking, respectively. While the yellow and blue regions are indicative of tough and brittle DN gels fracturing in the necking and preyielding regimes, respectively. Figures (a-d) have the same legend.

2. Behaviors of DN gels with Different Chemical Structures in the First Network

The above findings elucidated that the mechanical behaviors of DN gels depend on the topological structure of the two networks. To verify the universality of these scaling relationships observed in DN gels, we extended our investigation to DN gels featuring diverse hydrophobic polyelectrolyte (hPE) first networks (Figure 1c).

The nominal stress-stretch ratio curves and Mooney plots for the as-prepared SN gels are shown in Figures S6 and S7, respectively. The mechanical parameters (shear modulus, fracture stress, fracture stretch ratio) and efficiency of cross-linking reaction to form elastically effective strands are presented in Figures S8 and S9, respectively. We observed that all these hPE SN gels exhibited comparable values of G_0, which increased almost linearly with increasing cross-linker concentration (Φ_x). The fracture behaviors of these SN gels exhibited similar dependence on $\nu_{e,0}$ (Figures S8b and S8c)

as those in Figures 3c and 3d. Moreover, we observed again that all these hPE SN gels have a slightly lower fracture stress and stretch ratio than those of PE SN gels. The swelling ratios of all hPE SN gels in AAm solutions are presented in Figure S10. The linear swelling ratios (λ_s) exhibited a significant decrease with increasing Φ_x (Figure S10a). Roughly, the linear swelling ratio (λ_s) and the strand density at the as-prepared state ($\nu_{e,0}$) also obey a scaling relationship of $\lambda_s \propto {\nu_{e,0}}^{-0.4}$ (Figure S10b), in similar to Figure 4b.

The nominal stress-stretch ratio curves for six sets of as-prepared DN gels are shown in Figure 11. In general, the six sets of DN gels exhibited typical DN mechanical behaviors as depicted in Figure 1a, because the range of $\nu_{e,1}$ for these six sets of DN gels (0.07 to 1.6 mol/m^3) is narrower compared to the broader range discussed in Section 1 (0.01 to 16 mol/m^3). We analyzed in detail the effects of $\nu_{e,1}$ (or $\nu_{e,2}/\nu_{e,1}$) on various characteristic mechanical parameters on these gels, and the results are shown in Figure S11-S13. Overall, despite the different chemical structures in the first network, the data points for all DN gels overlapped well for each characteristic parameter. We even observed more consistent scaling relationships with smaller deviations for these six sets of data due to the narrow range of $\nu_{e,1}$ investigated.

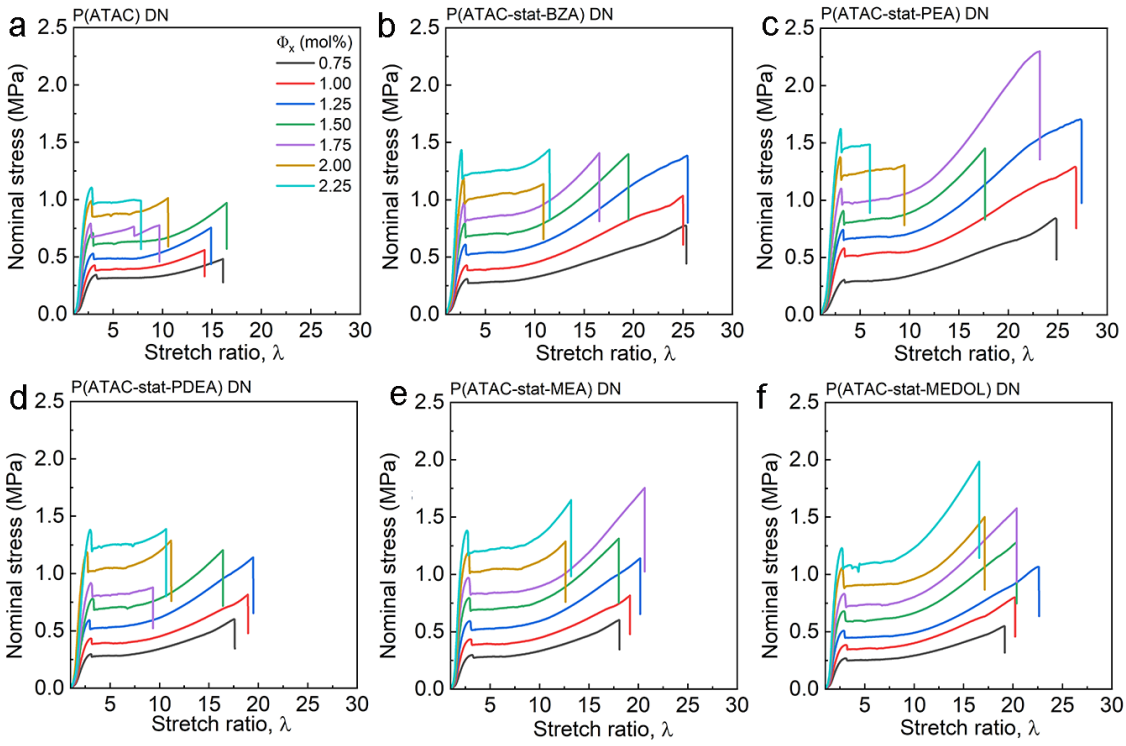

Figure 11. Tensile stress-stretch ratio curves of PE and hPE DN gels with varying cross-linker density (Φ_x) of the first network, while keeping the same formulation of the second network. The measurements were performed on the as-prepared DN gels.

Yielding behavior. The engineering yield stress (σ_y), yield stretch ratio (λ_y), and true yield stress ($\sigma_{T,y}$) of these DN gels as a function of the number density of the first network strands ($\nu_{e,1}$) are shown in Figures S11a-c. The corresponding normalized yielding stress (σ_Y), stretch ratio (λ_Y), and true yielding stress ($\sigma_{T,Y}$) as a function of the number density of the first network strands in the as-prepared state ($\nu_{e,0}$) are shown in Figures S11d-f. The scaling relationships of $\sigma_y \propto {\nu_{e,1}}^{0.58}$, $\lambda_y \propto {\nu_{e,1}}^{-0.05}$, $\sigma_{T,y} \propto {\nu_{e,1}}^{0.55}$ observed for these DN gels align closely with those observed in Figure

6. Again, the scaling relationships of $\sigma_Y \propto {\nu_{e,0}}^{0.5}$, $\lambda_Y \propto {\nu_{e,0}}^{-0.5}$, $\sigma_{T,Y} \propto {\nu_{e,0}}^{0}$, the same scaling relationship as that in Figure 7, are observed.

Plateau stress and necking of DN gels. The plateau stress (σ_p) against $\nu_{e,1}$ is presented in Figure S12a. Again, all data points overlapped on a scaling relationship of $\sigma_p \propto {\nu_{e,1}}^{0.58}$. The scaling exponent 0.58 is consistent with the observation of 0.57 in Figure 8a. The ratio of $\frac{\sigma_p}{\sigma_y}$ as a function of $\nu_{e,1}$ and $\frac{\nu_{e,2}}{\nu_{e,1}}$ depicted in Figure S12b also consistent with the results in Figure 8b.

Hardening and fracture behaviors of DN gels. Hardening stretch ratio (λ_h), degree of strain-hardening (κ), fracture stress (σ_f), and fracture stretch ratio (λ_f) for both DN gels against the chain density of the first network ($\nu_{e,1}$) are illustrated in Figure S13. The hardening stretch ratio slightly increases, and $\kappa \propto {\nu_{e,1}}^{0.63}$. Furthermore, $\sigma_f \propto {\nu_{e,1}}^{0.38}$. As $\nu_{e,1}$ increases, the fracture stretch ratio was constant (~20) for fractures occurring in hardening regime while decreases for fractures occurring in necking regime. All these results are consistent with the observations in Figure 10.

In summary, the characteristic mechanical behaviors of DN gels only depend on the topological structures of the two networks, independent of the chemical structure of the first network.

3. A comparison of yielding point with 1-D fracture model.

Our findings reveal that the mechanical properties of DN gels are predominantly governed by the topological structures of the two networks, with the chemical structure of the first network playing only a minimal role. In this section, we compare the scaling relationships for the yield with the theoretical fracture predictions from a 1-D fracture model. We assume that the yielding point corresponds to the fracture of the first network. The 1-D affine model describes the fracture of an ideally homogeneous network. [29] This network is characterized by Kuhn monomer number in each strand (N_x), the end-to-end distance of a strand (R_0), and the strand density ($\nu_{e,0}$) in the reference state. The strands adopt a Gaussian conformation, with $R_0 \simeq bN_x{}^{1/2}$, where b is the length of a Kuhn monomer. After swelling by a linear ratio (λ_s), the end-to-end distance of a strand (R) becomes $R = \lambda_s R_0$, and the strand density becomes $\nu_{e,1} = \nu_{e,0}\lambda_s{}^{-3}$. The 1-D affine model simply assumes that the network undergoes affine deformation with a constant volume, and that fracture occurs when the strands in the stretching direction reach their stretching limit. Thus, the maximum stretch ratio for a swollen network is given by $\lambda_{max} \simeq \frac{bN_x}{R} \simeq \frac{N_x{}^{1/2}}{\lambda_s}$. The maximum breaking stress is $\sigma_{max} \simeq \nu_{e,1} R f_b = \nu_{e,0} R_0 f_b \lambda_s{}^{-2}$. Here, f_b is the force required to break one network strand, and $\nu_{e,1}R$ is the number of strands per unit area. Since the Kuhn monomer concentration in the reference state is $C_0 = N_x \nu_{e,0}$, we have

$$\lambda_{max} \simeq \lambda_s{}^{-1}\left(\frac{C_0}{\nu_{e,0}}\right)^{1/2} \tag{6}$$

$$\sigma_{max} \simeq \lambda_s{}^{-2} f_b b C_0{}^{1/2} \nu_{e,0}{}^{1/2} \tag{7}$$

$$\sigma_{T,max} \equiv \sigma_{max}\lambda_{max} \simeq f_b b C_0 {\lambda_s}^{-3} \quad (8)$$

Using this 1-D model and swelling behavior of the first network, we can explain the weak dependence of the yielding stretch ratio λ_y on $\nu_{e,1}$ in Figures 6b and S11b. In Figures 4b and S10b, we observed a scaling relationship of $\lambda_s \propto {\nu_{e,0}}^{-0.4}$, regardless of the differences in chemical structure. From this scaling relation, one obtains $R \sim {N_x}^{0.9}$ by combining $C_0 = N_x \nu_{e,0}$ and $R = \lambda_s R_0 \simeq \lambda_s b {N_x}^{1/2}$. This result indicates that the polymer strands are very close to their fully extended state in these water-swollen gels. For such gels, the maximum stretch ratio is $\lambda_{max} \simeq \frac{bN_x}{R} \sim \frac{N_x}{{N_x}^{0.9}} \sim {N_x}^{0.1} \sim {\nu_{e,1}}^{-0.05}$. Here, we used the relation $\nu_{e,1} = \nu_{e,0}{\lambda_s}^{-3} \sim {\nu_{e,0}}^{2.2}$.

The 1-D affine model gives rise to relationships between the theoretical fracture point and the network structure at the reference state, [8] as

$$\lambda_{max,0} = \left(\frac{C_0}{\nu_{e,0}}\right)^{1/2} \quad (9)$$

$$\sigma_{max,0} = f_b b {C_0}^{1/2} {\nu_{e,0}}^{1/2} \quad (10)$$

$$\sigma_{T,max,0} \equiv \sigma_{max,0}\lambda_{max,0} = f_b b C_0 \quad (11)$$

The relationships $\lambda_{max,0} \propto {\nu_{e,0}}^{-0.5}$ and $\sigma_{max,0} \propto {\nu_{e,0}}^{0.5}$ are consistent with scaling relationships for the yielding stretch ratio $\lambda_Y \propto {\nu_{e,0}}^{-0.5}$ and yielding stress $\sigma_Y \propto {\nu_{e,0}}^{0.5}$ observed in this study. Furthermore, Equation-11 tells that the maximum true stress $\sigma_{T,max,0}$ increases with the Kuhn monomer concentration C_0 of the network, independent of $\nu_{e,0}$. This is also consistent with our observation ($\sigma_{T,Y} \propto {\nu_{e,0}}^0 C_m$) (Figures 7c and 7d). In addition, Equations 9 and 10 suggest that the breaking engineering stress $\sigma_{max,0}$, and the maximum stretch ratio $\lambda_{max,0}$ depend on the Kuhn

monomer concentration. This explains the relatively large dispersion observed in the relationship between the yield point and strand density when the monomer concentration was altered in Section 1, particularly for the yield stretch ratio (Figure 7b). Consequently, we plotted σ_Y against ${C_0}^{1/2}{\nu_{e,0}}^{1/2}$ and λ_Y against ${C_0}^{1/2}/{\nu_{e,0}}^{1/2}$. Here, we assume that all monomers are polymerized into elastically effective strands, and the Kuhn monomer concentration can be expressed as $C_0 = C_m a/b$. Moreover, we adopted the reported values for the average monomer size ($a = 0.25$ nm) [40-42] and a typical Kuhn monomer length ($b = 0.5$ nm) [31, 43] for vinyl polymers. As detailed in Figure 12, except for large values of ${C_0}^{1/2}/{\nu_{e,0}}^{1/2}$, all data points almost fall on a straight line. These agreement between the correlations of yielding and network structure, and the correlations from the 1-D affine model for fracture, provides evidence for the efficacy of the 1-D affine model in explaining the fracture behavior of the first networks in DN gels.

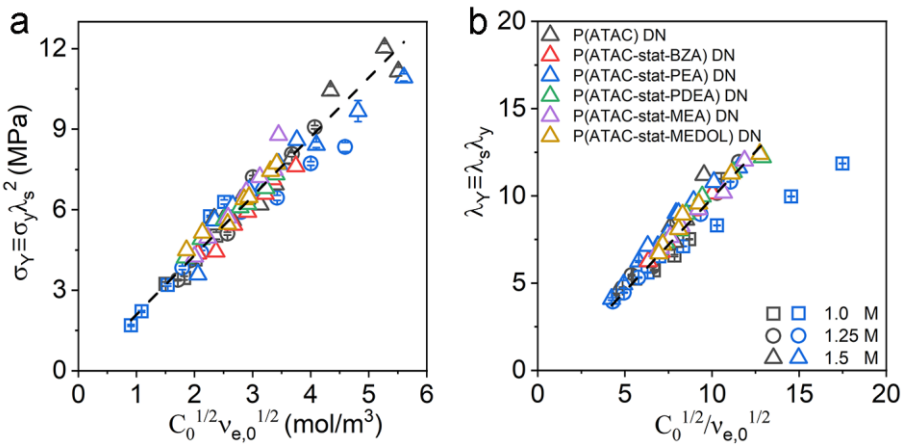

Figure 12. (a) Dependence of σ_Y ($\sigma_Y \equiv \sigma_y {\lambda_s}^2$) on ${C_0}^{1/2}{\nu_{e,0}}^{1/2}$. (b) Dependence of λ_Y ($\lambda_Y \equiv \lambda_s \lambda_y$) on ${C_0}^{1/2}/{\nu_{e,0}}^{1/2}$. Both figures utilize the same legend. The variation in data point color signifies DN gels with differing chemical structures in the first network, while the diversity in data point shape indicates variations in the monomer concentration of the first network. The dashed lines are a guide to the eyes.

Based on these findings, we attempt to make a semi-quantitative comparison between the experimental observations (σ_Y, λ_Y and $\sigma_{T,Y}$) and the predictions derived from 1-D affine model ($\sigma_{max,0}$, $\lambda_{max,0}$ and $\sigma_{max,0}\lambda_{max,0}$). For theoretical calculations, we adopted the force required to break a single network strand ($f_b = 3.2\ nN$) at the observation time scale. [44] In Figure 13, we present the experimental-to-theoretical ratio for fracture stretch ratio ($\lambda_Y/\lambda_{max,0}$), fracture stress ($\sigma_Y/\sigma_{max,0}$), and true fracture stress ($\sigma_{T,Y}/\sigma_{T,max,0}$) for the first network in DN gels. Notably, despite the broad range of chain densities (0 to 40 mol/m^3) explored, the experimental-to-theoretical ratio remains remarkably constant. While directly comparing experimental data to the scaling theory of 1-D affine model presents challenges due to inherent complexities, our analysis yields approximate ratio values. Specifically, the values of $\lambda_Y/\lambda_{max,0}$ are remarkably close to 1, suggesting that the yield point corresponds to the average stretching limit of the first network, independent of their chemical structures (Figure 13a). On the other hand, the ratio for normalized engineering yield stress ($\sigma_Y/\sigma_{max,0}$) and normalized true yield stress ($\sigma_{T,Y}/\sigma_{T,max,0}$) are around 0.075 (Figures 13b and 13c).

One reason for such large discrepancy is probably due to the localized stress concentration within the first network. Although the second network plays a role in stress dispersion and mitigation around the internal crack tip of the first network, it does not fully counteract stress concentration effects. A systematic analysis and in-depth examination of the localized stress concentration will be discussed in forthcoming papers.

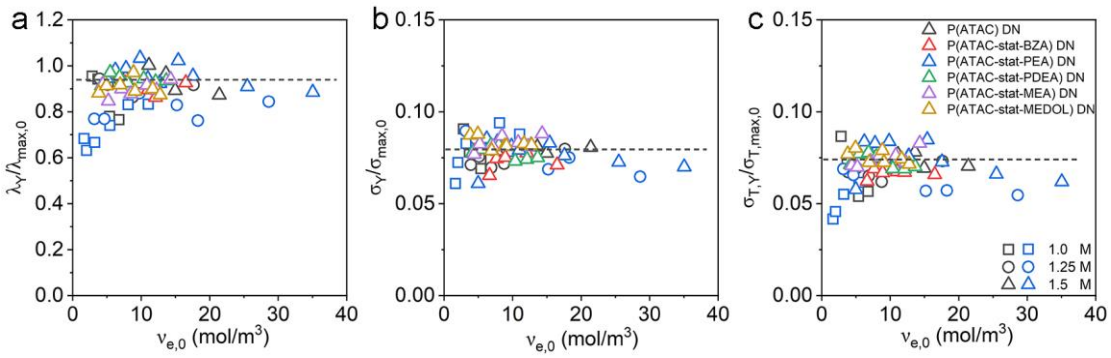

Figure 13. Comparison of the yielding point of DN gels with the theoretical fracture point of the first network. (a) Ratio of the normalized yield stretch ratio (λ_Y) to the calculated fracture stretch ratio ($\lambda_{max,0}$) for DN gels. (b) Ratio of the normalized engineering yield stress (σ_Y) to the calculated fracture stress ($\sigma_{max,0}$) for DN gels. (c) Ratio of the normalized true yield stress ($\sigma_{T,Y}$) to the calculated true stress ($\sigma_{T,max,0}$) for DN gels. All figures have the same legend. The variation in data point color signifies DN gels with differing chemical structures in the first network, while the diversity in data point shape indicates variations in the monomer concentration of the first network. The dashed lines are a guide to the eyes.

SUMMARY AND CONCLUSIONS

We observed four categories of tensile behavior of DN gels, arising from changes in the topological structure of the first network while maintaining a constant second network. These structural changes alter the mechanical balance between the two networks, independently of the first network's chemical composition: 1) Brittle DN gels ($\frac{\nu_{e,2}}{\nu_{e,1}} < 1.5\sim4.8$). The second network is too weak to maintain the integrity of the entire sample when the first network undergoes internal fractures, resulting in material fracture before yielding. 2) Tough DN gels ($1.5\sim4.8 < \frac{\nu_{e,2}}{\nu_{e,1}} < 21$). These DN gels exhibit clear yielding and necking. The strengths of the two networks are closely matched, with fractures occurring in the necking regime. 3) Optimized DN gels ($21 < \frac{\nu_{e,2}}{\nu_{e,1}} < 400$). DN gels in this category show clear yielding, necking, and hardening. The second network is stronger than the first, leading to fractures occurring in the hardening regime. 4) Over-supported DN gels ($\frac{\nu_{e,2}}{\nu_{e,1}} > 400$). The strength of the second network far exceeds that of the first, significantly reducing stress concentration in the first network. The internal fracture mode of the first network transitions from localized initial breaks into discontinuous structures, expanding to encompass the entire material when $\frac{\nu_{e,2}}{\nu_{e,1}}$<400, to more widespread and delocalized fractures in the entire material when $\frac{\nu_{e,2}}{\nu_{e,1}}$>400. Stress increases as stretching progresses, with fracture occurring in the hardening regime.

For the three categories of ductile DN gels, we observed universal scaling relationships between characteristic tensile parameters and the average strand density of the first network ($\nu_{e,1}$) in the virgin DN gels.

(1) Yielding point: Primarily governed by the first network, with the engineering yield stress, yield stretch ratio, and true yield stress following specific scaling relationships of $\sigma_y \propto {\nu_{e,1}}^{0.58}$, $\lambda_y \propto {\nu_{e,1}}^{-0.07}$, and $\sigma_{T,y} \propto {\nu_{e,1}}^{0.55}$, respectively. Since these relationships are implicitly correlated with the relationship between the swelling ratio (λ_s) and elastic strand density at reference state ($\nu_{e,0}$) of the first network, we normalized the yielding parameters of DN gels to the as-prepared state (reference state) of the first network. The corresponding scaling relationships at the reference state follow $\sigma_Y \propto {\nu_{e,0}}^{0.5}$, $\lambda_Y \propto {\nu_{e,0}}^{-0.5}$, and $\sigma_{T,Y} \propto {\nu_{e,0}}^{0} C_m$. These scaling relationships are consistent with our previous findings and can be explained by a theoretical 1-D affine model for the fracture of a homogeneous network composed of Gaussian strands.

(2) Necking regime: In this regime, where necked and un-necked regions coexist, the plateau stress primarily depends on the topological structure of the first network, following a scaling relationship of $\sigma_p \propto {\nu_{e,1}}^{0.58}$. The normalized plateau stress at reference state of the first network is $\sigma_P \propto {\nu_{e,0}}^{0.45}$, similar to $\sigma_Y \propto {\nu_{e,0}}^{0.5}$. Meanwhile, the hardening stretch ratio λ_h shows a slightly increasing trend with $\nu_{e,1}$.

(3) Hardening Regime: Governed by both the first and the second networks. The degree of strain-hardening follows the relation $\kappa \propto {\nu_{e,1}}^{0.61}$, and the fracture stress scales as $\sigma_f \propto {\nu_{e,1}}^{0.41}$. These results suggest that even when the first network fractures

into "clusters" in this regime, it still plays a significant role in load-bearing by functioning as slidable cross-linkers.

We note that the critical number density ratios of the two networks required for different tensile responses apply to a fixed strand length of the second network. Variations in the extensibility of the second network would alter these boundary values, a factor that will be explored in future studies.

ASSOCIATED CONTENT

Supporting Information.

The following files are available free of charge.

Mooney plots for P(ATAC) and P(ATAC-stat-PEA) SN gels, stress-stretch ratio curve and Mooney plot for the second network (Figure S1), efficiency of cross-linking reaction in forming elastically effective strands in P(ATAC) and P(ATAC-stat-PEA) SN gels at different monomer concentrations (Figure S2), tensile stress-stretch ratio curves and birefringence images of four representative P(ATAC-stat-PEA) DN gels with different $\nu_{e,1}$ (Figure S3), characteristic mechanical parameters σ_y, λ_y, σ_p, λ_h, σ_f, and λ_f derived from the stress-stretch ratio curves of P(ATAC) and P(ATAC-stat-PEA) DN gels (Figure S4), the ratio of the number density of elastically effective strands between the second ($\nu_{e,2}$) and the first ($\nu_{e,1}$) networks ($\nu_{e,2}/\nu_{e,1}$) in DN gels (Figure S5). Stress-stretch ratio curves (Figure S6), Mooney plots (Figure S7), shear

modulus G_0, number density of elastically effective strands $\nu_{e,0}$, fracture stress $\sigma_{SN,f}$, and fracture stretch ratio $\lambda_{SN,f}$ (Figure S8), efficiency of cross-linking reaction in forming elastically effective strands (Figure S9), and linear swelling ratio λ_s (Figure S10) of SN gels with various chemical structures. Yielding behaviors of six sets of DN gels with varying chemical structures of the first network (Figure S11), plateau stress (σ_p) and ratio of plateau stress to yielding stress ($\frac{\sigma_p}{\sigma_y}$) (Figure S12), hardening stretch ratio λ_h, degree of strain-hardening κ, fracture stress σ_f, and fracture stretch ratio λ_f for DN gels with different chemical structures of the first network (Figure S13). (PDF)

Birefringence of tensile process for over-supported (Video S1), optimized (Video S2), tough (Video S3), and brittle (Video S4) P(ATAC-stat-PEA) DN gels. Birefringence of tensile process for un-damaged (Video S5) and pre-damaged (Video S6) P(ATAC) DN gels with low $\nu_{e,2}/\nu_{e,1}$. Birefringence for un-damaged (Video S7) and pre-damaged (Video S8) P(ATAC) DN gels with high $\nu_{e,2}/\nu_{e,1}$. (Video)

AUTHOR INFORMATION

Corresponding Author

Hailong Fan − *Institute for Chemical Reaction Design and Discovery (WPI-ICReDD), Hokkaido University, Sapporo 001-0021, Japan;* orcid.org/0000-0002-4900-1421; Email: fanhl@icredd.hokudai.ac.jp

Jian Ping Gong – *Institute for Chemical Reaction Design and Discovery (WPI-ICReDD), Hokkaido University, Sapporo 001-0021, Japan; Faculty of Advanced Life*

Science, Hokkaido University, Sapporo 001-0021, Japan; orcid.org/0000-0003-2228-2750; Email: gong@sci.hokudai.ac.jp

Authors

Feixue Lu – *Graduate School of Life Science, Hokkaido University, Sapporo 001-0021, Japan;* orcid.org/0000-0001-7133-273X

Tasuku Nakajima – *Institute for Chemical Reaction Design and Discovery (WPI-ICReDD), Hokkaido University, Sapporo 001-0021, Japan; Faculty of Advanced Life Science, Hokkaido University, Sapporo 001-0021, Japan;* orcid.org/0000-0002-2235-3478

Yong Zheng – *Institute for Chemical Reaction Design and Discovery (WPI-ICReDD), Hokkaido University, Sapporo 001-0021, Japan;* orcid.org/0000-0002-9445-1229

Notes

The authors declare no conflicts of interests.

ACKNOWLEDGMENTS

This research was supported by the Japan Society for the Promotion of Science (JSPS) KAKENHI (grant number JP22H04968, JP22K21342, and JP24K17728). F.X. Lu thanks the MEXT, Japan for scholarship. Institute for Chemical Reaction Design and Discovery (WPI-ICReDD) was established by World Premier International Research Initiative (WPI), MEXT, Japan. The authors thank Prof. Michael Rubinstein in Duke University for insightful discussion.

REFERENCES

(1) Xu, X.; Jerca, V. V.; Hoogenboom, R. Bioinspired double network hydrogels: from covalent double network hydrogels via hybrid double network hydrogels to physical double network hydrogels. Materials Horizons **2021**, 8, 1173-1188. DOI: 10.1039/D0MH01514H.

(2) Zheng, Y.; Jiang, J.; Jin, M.; Miura, D.; Lu, F. X.; Kubota, K.; Nakajima, T.; Maeda, S.; Ito, H.; Gong, J. P. In Situ and Real-Time Visualization of Mechanochemical Damage in Double-Network Hydrogels by Prefluorescent Probe via Oxygen-Relayed Radical Trapping. Journal of the American Chemical Society **2023**, 145, 7376-7389. DOI: 10.1021/jacs.2c13764.

(3) Gong, J.; Katsuyama, Y.; Kurokawa, T.; Osada, Y. Double-network hydrogels with extremely high mechanical strength. Advanced Materials **2003**, 15, 1155-1158. DOI: 10.1002/adma.200304907.

(4) Matsuda, T.; Kawakami, R.; Nakajima, T.; Hane, Y.; Gong, J. P. Revisiting the Origins of the Fracture Energy of Tough Double-Network Hydrogels with Quantitative Mechanochemical Characterization of the Damage Zone. Macromolecules **2021**, 54, 10331-10339. DOI: 10.1021/acs.macromol.1c01214.

(5) Zheng, Y.; Wang, Y.; Nakajima, T.; Gong, J. P. Effect of Predamage on the Fracture Energy of Double-Network Hydrogels. ACS Macro Letters **2024**, 13, 130-137. DOI: 10.1021/acsmacrolett.3c00702.

(6) Jia, Y.; Zhou, Z.; Jiang, H.; Liu, Z. Characterization of fracture toughness and damage zone of double network hydrogels. Journal of the Mechanics and Physics of Solids **2022**, 169, 105090. DOI: 10.1016/j.jmps.2022.105090.

(7) You, J.; Liu, Z. Revealing novel insights into the toughening mechanism of double network hydrogels via uniaxial tensile tests. Journal of the Mechanics and Physics of Solids **2024**, 190, 105710. DOI: 10.1016/j.jmps.2024.105710.

(8) Zheng, Y.; Nakajima, T.; Cui, W.; Hui, C.-Y.; Gong, J. P. Swelling Effect on the Yielding, Elasticity, and Fracture of Double-Network Hydrogels with an

Inhomogeneous First Network. Macromolecules **2023**, 56, 3962–3972. DOI: 10.1021/acs.macromol.3c00354.

(9) Zhu, P.; Zhong, Z. Development of the network alteration theory for the Mullins softening of double-network hydrogels. Mechanics of Materials **2021**, 152, 103658. DOI: 10.1016/j.mechmat.2020.103658.

(10) Fukao, K.; Nakajima, T.; Nonoyama, T.; Kurokawa, T.; Kawai, T.; Gong, J. P. Effect of Relative Strength of Two Networks on the Internal Fracture Process of Double Network Hydrogels As Revealed by in Situ Small-Angle X-ray Scattering. Macromolecules **2020**, 53, 1154-1163. DOI: 10.1021/acs.macromol.9b02562.

(11) Ogouari, L.; Guo, Q.; Zaïri, F.; Mai, T.-T.; Gong, J. P.; Urayama, K. A multiscale model for the multiaxial anisotropic damage of double-network gels. Mechanics of Materials **2024**, 196, 105058. DOI: 10.1016/j.mechmat.2024.105058.

(12) Morovati, V.; Saadat, M. A.; Dargazany, R. Necking of double-network gels: Constitutive modeling with microstructural insight. Physical Review E **2020**, 102, 062501. DOI: 10.1103/PhysRevE.102.062501.

(13) Nakajima, T.; Kurokawa, T.; Ahmed, S.; Wu, W.; Gong, J. Characterization of internal fracture process of double network hydrogels under uniaxial elongation. Soft Matter **2013**, 9, 1955-1966. DOI: 10.1039/c2sm27232f.

(14) Zhu, P.; Zhong, Z. Modelling the mechanical behaviors of double-network hydrogels. International Journal of Solids and Structures **2020**, 193-194, 492-501. DOI: 10.1016/j.ijsolstr.2020.03.003.

(15) Matsuda, T.; Nakajima, T.; Fukuda, Y.; Hong, W.; Sakai, T.; Kurokawa, T.; Chung, U.-i.; Gong, J. P. Yielding Criteria of Double Network Hydrogels. Macromolecules **2016**, 49, 1865-1872. DOI: 10.1021/acs.macromol.5b02592.

(16) Tanaka, Y. A local damage model for anomalous high toughness of double-network gels. Europhysics Letters **2007**, 78, 56005. DOI: 10.1209/0295-5075/78/56005.

(17) Brown, H. A model of the fracture of double network gels. Macromolecules **2007**, 40, 3815-3818. DOI: 10.1021/ma062642y.

(18) Chae, M.-K.; Lee, N.-K.; Jung, Y.; Joanny, J. F.; Johner, A. Structure of a Hydrophobic Polyelectrolyte Chain with a Random Sequence. Macromolecules **2022**, 55, 6275-6285. DOI: 10.1021/acs.macromol.2c00779.

(19) Landsgesell, J.; Nová, L.; Rud, O.; Uhlík, F.; Sean, D.; Hebbeker, P.; Holm, C.; Košovan, P. Simulations of ionization equilibria in weak polyelectrolyte solutions and gels. Soft Matter **2019**, 15, 1155-1185. DOI: 10.1039/C8SM02085J.

(20) Dobrynin, A. V.; Rubinstein, M. Hydrophobic Polyelectrolytes. Macromolecules **1999**, 32, 915-922. DOI: 10.1021/ma981412j.

(21) Ben Mahmoud, S.; Essafi, W.; Brûlet, A.; Boué, F. How Necklace Pearls Evolve in Hydrophobic Polyelectrolyte Chains under Good Solvent Addition: A SANS Study of the Conformation. Macromolecules **2018**, 51, 9259-9275. DOI: 10.1021/acs.macromol.8b00990.

(22) Fan, H. L.; Wang, J. H.; Tao, Z.; Huang, J. C.; Rao, P.; Kurokawa, T.; Gong, J. P. Adjacent cationic-aromatic sequences yield strong electrostatic adhesion of hydrogels in seawater. Nature Communications **2019**, 10, 5127. DOI: 10.1038/s41467-019-13171-9.

(23) Fan, H.; Cai, Y.; Gong, J. P. Facile tuning of hydrogel properties by manipulating cationic-aromatic monomer sequences. Science China Chemistry **2021**, 64, 1560-1568. DOI: 10.1007/s11426-021-1010-3.

(24) Fan, H.; Wang, J.; Gong, J. P. Barnacle Cement Proteins-Inspired Tough Hydrogels with Robust, Long-Lasting, and Repeatable Underwater Adhesion. Advanced Functional Materials **2021**, 31, 2009334. DOI: 10.1002/adfm.202009334.

(25) Fan, H.; Naohara, D.; Li, W.; Li, X.; Gong, J. P. Tuning network structures of hydrophobic hydrogels by controlling polymerization solvent. Polymer Chemistry **2024**, 15, 2104-2111. DOI: 10.1039/D4PY00256C.

(26) Nakajima, T.; Kurokawa, T.; Furukawa, H.; Gong, J. P. Effect of the constituent networks of double-network gels on their mechanical properties and energy dissipation process. Soft Matter **2020**, 16, 8618-8627. DOI: 10.1039/d0sm01057j.

(27) Yoshida, M.; Kiyama, R.; Zhang, Y.; King, D. R.; Kurokawa, T.; Gong, J. P. Preyielding and necking process of double network hydrogels revealed by sample geometry effects. Extreme Mechanics Letters **2024**, 69, 102163. DOI: 10.1016/j.eml.2024.102163.

(28) Zheng, Y.; Matsuda, T.; Nakajima, T.; Cui, W.; Zhang, Y.; Hui, C.-Y.; Kurokawa, T.; Gong, J. P. How chain dynamics affects crack initiation in double-network gels. Proceedings of the National Academy of Sciences **2021**, 118, e2111880118. DOI: doi:10.1073/pnas.2111880118.

(29) Rubinstein, M.; Colby, R. H. Polymer physics. vol. 23 Oxford University Press. New York 2003.

(30) Lin, T.-S.; Wang, R.; Johnson, J. A.; Olsen, B. D. Revisiting the Elasticity Theory for Real Gaussian Phantom Networks. Macromolecules **2019**, 52, 1685-1694. DOI: 10.1021/acs.macromol.8b01676.

(31) Kiyama, R.; Yoshida, M.; Nonoyama, T.; Sedlačík, T.; Jinnai, H.; Kurokawa, T.; Nakajima, T.; Gong, J. P. Nanoscale TEM Imaging of Hydrogel Network Architecture. Advanced Materials **2023**, 35, 2208902. DOI: 10.1002/adma.202208902.

(32) Nakajima, T.; Furukawa, H.; Tanaka, Y.; Kurokawa, T.; Osada, Y.; Gong, J. True Chemical Structure of Double Network Hydrogels. Macromolecules **2009**, 42, 2184-2189. DOI: 10.1021/ma802148p.

(33) Zhao, X. Multi-scale multi-mechanism design of tough hydrogels: building dissipation into stretchy networks. Soft Matter **2014**, 10, 672-687. DOI: 10.1039/C3SM52272E.

(34) Creton, C.; Ciccotti, M. Fracture and adhesion of soft materials: a review. Reports on Progress in Physics **2016**, 79, 046601. DOI: 10.1088/0034-4885/79/4/046601.

(35) Long, R.; Hui, C.-Y.; Gong, J. P.; Bouchbinder, E. The Fracture of Highly Deformable Soft Materials: A Tale of Two Length Scales. Annual Review of Condensed Matter Physics **2021**, 12, 71-94. DOI: 10.1146/annurev-conmatphys-042020-023937.

(36) Rinaldi, D.; Hamaide, T.; Graillat, C.; D'Agosto, F.; Spitz, R.; Georges, S.; Mosquet, M.; Maitrasse, P. RAFT copolymerization of methacrylic acid and poly(ethylene glycol) methyl ether methacrylate in the presence of a hydrophobic chain transfer agent in organic solution and in water. Journal of Polymer Science Part A: Polymer Chemistry **2009**, 47, 3045-3055. DOI: 10.1002/pola.23374.

(37) Ju, A.; Yu, H.; Yan, Y.; Cao, M.; Liu, J.; Liu, B. A high molecular weight acrylonitrile copolymer prepared by mixed solvents polymerization: II. effect of DMSO/water ratios on polymerization and stabilization. Journal of Polymer Research **2016**, 23, 208. DOI: 10.1007/s10965-016-1103-5.

(38) Kim, J.; Zhang, G.; Shi, M.; Suo, Z. Fracture, fatigue, and friction of polymers in which entanglements greatly outnumber cross-links. Science **2021**, 374, 212-216. DOI: 10.1126/science.abg6320.

(39) Zheng, D.; Lin, S.; Ni, J.; Zhao, X. Fracture and fatigue of entangled and unentangled polymer networks. Extreme Mechanics Letters **2022**, 51, 101608. DOI: 10.1016/j.eml.2022.101608.

(40) Na, Y. H.; Kurokawa, T.; Katsuyama, Y.; Tsukeshiba, H.; Gong, J. P.; Osada, Y.; Okabe, S.; Karino, T.; Shibayama, M. Structural characteristics of double network gels with extremely high mechanical strength. Macromolecules **2004**, 37, 5370-5374. DOI: 10.1021/ma049506i.

(41) Dou, S.; Colby, R. H. Charge density effects in salt-free polyelectrolyte solution rheology. Journal of Polymer Science Part B: Polymer Physics **2006**, 44, 2001-2013. DOI: 10.1002/polb.20853.

(42) Fischer, K.; Schmidt, M. Solvent-Induced Length Variation of Cylindrical Brushes. Macromolecular Rapid Communications **2001**, 22, 787-791. DOI: 10.1002/1521-3927(20010701)22:10<787::AID-MARC787>3.0.CO;2-Y.

(43) Cui, S.; Liu, C.; Wang, Z.; Zhang, X.; Strandman, S.; Tenhu, H. Single Molecule Force Spectroscopy on Polyelectrolytes: Effect of Spacer on Adhesion Force and Linear Charge Density on Rigidity. Macromolecules **2004**, 37, 946-953. DOI: 10.1021/ma0353991.

(44) Wang, Z. J.; Jiang, J.; Mu, Q.; Maeda, S.; Nakajima, T.; Gong, J. P. Azo-Cross-linked Double-Network Hydrogels Enabling Highly Efficient Mechanoradical Generation. Journal of the American Chemical Society **2022**, 144, 3154-3161. DOI: 10.1021/jacs.1c12539.